Collapse and black hole formation in magnetized, differentially rotating neutron stars

B C Stephens[1], M D Duez[1,3], Y T Liu[1], S L Shapiro[1,4] and M Shibata[2]

[1] Department of Physics, University of Illinois at Urbana-Champaign, Urbana, IL 61801, USA
[2] Graduate School of Arts and Sciences, University of Tokyo, Komaba, Meguro,
Tokyo 153-8902, Japan

Abstract
The capacity to model magnetohydrodynamical (MHD) flows in dynamical, strongly curved spacetimes significantly extends the reach of numerical relativity in addressing many problems at the forefront of theoretical astrophysics. We have developed and tested an evolution code for the coupled Einstein–Maxwell-MHD equations which combines a BSSN solver with a high resolution shock capturing scheme. As one application, we evolve magnetized, differentially rotating neutron stars under the influence of a small seed magnetic field. Of particular significance is the behaviour found for hypermassive neutron stars (HMNSs), which have rest masses greater than the mass limit allowed by uniform rotation for a given equation of state. The remnant of a binary neutron star merger is likely to be a HMNS. We find that magnetic braking and the magnetorotational instability lead to the collapse of HMNSs and the formation of rotating black holes surrounded by massive, hot accretion tori and collimated magnetic field lines. Such tori radiate strongly in neutrinos, and the resulting neutrino–antineutrino annihilation (possibly in concert with energy extraction by MHD effects) could provide enough energy to power short-hard gamma-ray bursts. To explore the range of outcomes, we also evolve differentially rotating neutron stars with lower masses and angular momenta than the HMNS models. Instead of collapsing, the non-hypermassive models form nearly uniformly rotating central objects which, in cases with significant angular momentum, are surrounded by massive tori.

PACS numbers: 04.25.Dm, 94.30.cq, 95.30.Qd, 97.60.Bw

[3] Present address: Center for Radiophysics Space Research Cornell University, Ithaca, NY 14853, USA.
[4] Also at the Department of Astronomy and NCSA, University of Illinois at Urbana–Champaign, Urbana, IL 61801, USA.

1. Introduction

Differential rotation is likely to be the norm in many astrophysical settings. For example, differentially rotating neutron stars can form from the collapse of massive stellar cores, which acquire rapid differential rotation during collapse even if they are spinning uniformly at the outset [1, 2] (see also [3]). Differential rotation can also arise from the mergers of binary neutron stars [4–6]. In these new-born, dynamically stable, neutron stars, magnetic fields and/or viscosity will transport angular momentum and substantially change the configurations on a secular timescale.

Some newly formed differentially rotating neutron stars may be *hypermassive*. The mass limits for non-rotating stars (the Oppenheimer–Volkoff limit) and for rigidly rotating stars (the *supramassive* limit, which is only about 20% larger) can be significantly exceeded by the presence of *differential* rotation [7, 8]. Mergers of binary neutron stars could lead to the formation of such hypermassive neutron stars (HMNSs) as remnants. The latest binary neutron star merger simulations in full general relativity [9–11] have confirmed that HMNS formation is indeed a possible outcome. HMNSs could also result from the core collapse of massive stars. Differentially rotating stars tend to approach rigid rotation when acted upon by processes which transport angular momentum. HMNSs, however, cannot settle down to rigidly rotating neutron stars since their masses exceed the maximum allowed by rigid rotation. Thus, delayed collapse to a black hole and, possibly, mass loss may result.

The merger of binary neutron stars has been proposed for many years as an explanation of short-hard GRBs [12, 13]. According to this scenario, after the merger, a stellar-mass black hole is formed, surrounded by hot accretion torus containing $\sim$1–10% of the total mass of the system. The GRB fireball is then powered by energy extracted from this system, either by MHD processes or emission from neutrino–antineutrino annihilation. The viability of this model depends on the presence of a significantly massive accretion disc after the collapse of the remnant core, which in turn depends on the mechanism driving the collapse.

Though magnetic fields likely play a significant role in the evolution of HMNSs, the numerical tools needed to study this problem have not been available until recently. In particular, the evolution of magnetized HMNSs can only be determined by solving the coupled Einstein–Maxwell-MHD equations self-consistently in full general relativity. Recently, Duez *et al* [14] and Shibata and Sekiguchi [15] independently developed codes designed to do such calculations for the first time (see also [16, 17]). The first simulations of magnetized hypermassive neutron star collapse (assuming both axial and equatorial symmetry) were reported in [18], and the implications of these results for short GRBs were presented in [19]. These simulations proved that the amplification of small seed magnetic fields by a combination of magnetic winding and the magnetorotational instability (MRI) [20, 21] is sufficient to trigger collapse in hypermassive stars on the Alfvén timescale, confirming earlier predictions [7, 22].

We also compare the results for hypermassive stars with the evolution of two differentially rotating models below the supramassive limit in order to highlight the qualitatively different physical effects which arise in the evolution. Given a fixed equation of state (EOS), the sequence of uniformly rotating stars with a given rest mass has a maximum angular momentum J_{max}. A non-hypermassive star having angular momentum $J > J_{max}$ is referred to as an 'ultraspinning' star. We perform simulations on the MHD evolution of two non-hypermassive stars—one is ultraspinning and the other is not; we refer to the latter as 'normal.' Instead of collapsing, they evolve to a new equilibrium state after several Alfvén times. The normal star settles down to a uniformly rotating configuration. In contrast, the ultraspinning star

Table 1. Initial models.

Case	$M_0/M_{0,\mathrm{TOV}}$[a]	$M_0/M_{0,\mathrm{sup}}$[b]	R_{eq}/M[c]	J/M^2[d]	$T_{\mathrm{rot}}/|W|$[e]	$\Omega_{\mathrm{eq}}/\Omega_c$[f]
A	1.69	1.46	4.48	1.0	0.249	0.33
B1	0.99	0.86	8.12	1.0	0.181	0.40
B2	0.98	0.85	4.84	0.38	0.040	0.34

[a] The ratio of the rest mass M_0 to the TOV rest mass limit for the given EOS.
[b] The ratio of the rest mass M_0 to the rest mass limit for uniformly rotating stars of the given EOS (the supramassive limit). If this ratio is greater than unity, the star is hypermassive.
[c] The equatorial coordinate radius R_{eq} normalized by the ADM mass.
[d] The ratio of the angular momentum J to M^2 (the angular momentum parameter).
[e] The ratio of the rotational kinetic energy to the gravitational binding energy.
[f] The ratio of the angular velocity at the equator to the central angular velocity.

settles down to a nearly uniformly rotating central core, surrounded by a differentially rotating torus.

The key subtlety in all of these simulations is that the wavelengths of the MRI modes must be well resolved on the computational grid. Since this wavelength is proportional to the magnetic field strength, it becomes very difficult to resolve for small seed fields. However, the simulations reported here succeed in resolving the MRI. In what follows, we assume geometrized units such that $G = c = 1$.

2. Initial models

We consider three representative differentially rotating stars, which we call 'A', 'B1' and 'B2'. Their properties are listed in table 1. Star A is hypermassive while stars B1 and B2 are not. These configurations are all dynamically stable. All three models are constructed using a $\Gamma = 2$ polytropic EOS, $P = K\rho_0^\Gamma$, where P, K and ρ_0 are the pressure, polytropic constant and rest-mass density, respectively. The rest mass of star A exceeds the supramassive limit by 46%, while the rest masses of stars B1 and B2 are below the supramassive limit. The angular momentum of star B1 exceeds the maximum angular momentum (J_{max}) for a rigidly rotating star with the same rest mass and EOS, whereas star B2 has angular momentum $J < J_{\mathrm{max}}$. Thus, star B1 is 'ultraspinning,' while star B2 is 'normal'. These models may be scaled to any desired physical mass by adjusting the value of K [23].

Following previous papers (e.g., [7, 23–25]), we choose the initial rotation law $u^0 u_\varphi = A^2(\Omega_c - \Omega)$, where u^μ is the four-velocity, Ω_c is the angular velocity along the rotational axis and $\Omega \equiv u^\varphi/u^0$ is the angular velocity. The constant A has units of length and determines the steepness of the differential rotation. For these models, A is set equal to the coordinate equatorial radius R_{eq}. The corresponding values of $\Omega_{\mathrm{eq}}/\Omega_c$ are shown in table 1 (where Ω_{eq} is the angular velocity at the equatorial surface).

We must also specify initial conditions for the magnetic field. We choose to add a weak poloidal magnetic field to the equilibrium model by introducing a vector potential of the following form, $A_\varphi = \varpi^2 \max[A_b(P - P_{\mathrm{cut}}), 0]$, where the cutoff P_{cut} is 4% of the maximum pressure, and A_b is a constant which determines the initial strength of the magnetic field. We characterize the strength of the initial magnetic field by $C \equiv \max\left(B_{(u)}^2/(8\pi P)\right)$, i.e. the maximum value on the grid of the ratio of the magnetic energy density to the pressure (where $B_{(u)}^\mu$ refers to the magnetic field in the comoving frame of the fluid). We choose A_b such that $C \sim 10^{-3}$–10^{-2}. We have verified that such small initial magnetic fields introduce negligible violations of the Hamiltonian and momentum constraints in the initial data.

3. Numerical methods

Duez *et al* [14] and Shibata and Sekiguchi [15] have independently developed new codes to evolve magnetized fluids in dynamical spacetimes by solving the Einstein–Maxwell-MHD system of equations self-consistently. Several tests have been performed with these codes, including MHD shocks, nonlinear MHD wave propagation, magnetized Bondi accretion, MHD waves induced by linear gravitational waves and magnetized accretion onto a neutron star. Details of our techniques for evolving the Einstein–Maxwell-MHD system as well as tests can be found in [14, 15]. We have performed several simulations for identical initial data using both codes and found that the results are essentially the same. The simulations presented here assume axial and equatorial symmetry. We adopt the Cartoon method [26] for evolving the BSSN equations [27], and use cylindrical coordinates for evolving the induction and MHD equations. In this scheme, the coordinate x is identified with the cylindrical radius ϖ, and the y-direction corresponds to the azimuthal direction.

4. Results

4.1. Star A

We have performed simulations on star A with initial field strength given by $C = 2.5 \times 10^{-3}$. We use a uniform grid with size (N, N) in cylindrical coordinates (ϖ, z), which covers the region $[0, L]$ in each direction, where $L = 4.5R_{eq}$. For star A, $R_{eq} = 4.5M = 18.6$ km$(M/2.8M_\odot)$. To check the convergence of our numerical results, we perform simulations with four different grid resolutions: $N = 250, 300, 400$ and 500. Unless otherwise stated, all results presented in the following subsections are from the simulation data with resolution $N = 500$.

4.1.1. General features of the evolution.
Figure 1 shows snapshots of the density contours and poloidal magnetic field lines (lines of constant A_φ) in the meridional plane. In the early phase of the evolution, the frozen-in poloidal magnetic fields lines are wound up by the differentially rotating matter, creating a toroidal field which grows linearly in time (see figure 2(*d*)). When the magnetic field becomes sufficiently strong, magnetic stresses act back on the fluid, causing a redistribution of angular momentum. The core of the star contracts while the outer layers expand. As shown in figure 2(*c*), the effect of the MRI becomes evident for $t \gtrsim 6P_c$. This is manifested as a sudden increase in the maximum value of $|B^x|$ ($\equiv |B^\varpi|$), which grows exponentially for a short period (about one e-folding) before saturating. The effect of the MRI is also visible in figure 1, where we see distortions in the poloidal field lines. The amplitude of the toroidal field begins to decrease after $t \gtrsim 20P_c \sim t_A$ (see figure 2(*d*)) and the core of the star becomes less differentially rotating.

The combined effects of magnetic braking and the MRI eventually trigger gravitational collapse to a black hole at $t \approx 66P_c \approx 36(M/2.8M_\odot)$ ms, where P_c is the initial central rotation period. A collimated magnetic field forms near the polar region at this time (see figure 1). However, a substantial amount of toroidal field is still present. Without black hole excision, the simulation becomes inaccurate soon after the formation of the apparent horizon because of grid stretching. To follow the subsequent evolution, a simple excision technique is employed [28, 29]. We are able to track the evolution for another $300M \approx 8P_c$. We find that not all of the matter promptly falls into the black hole. The system settles down to a quasi-equilibrium state consisting of a black hole surrounded by a hot torus and a collimated
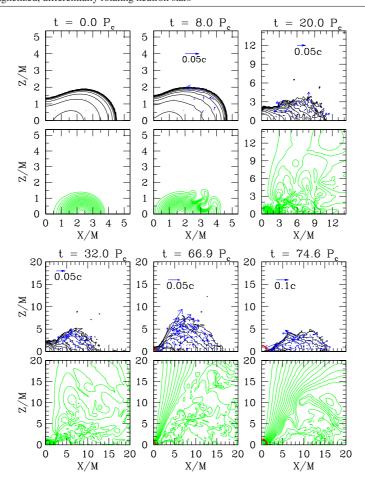
Figure 1. Snapshots of rest-mass density contours and poloidal magnetic field lines for star A at selected times. The first and third rows show snapshots of the rest-mass density contours and velocity vectors on the meridional plane. The second and fourth rows show the corresponding field lines (lines of constant A_φ) for the poloidal magnetic field at the same times. The density contours are drawn for $\rho_0/\rho_{max}(0) = 10^{-0.36i-0.09}(i = 0\text{–}10)$, where $\rho_{max}(0)$ is the maximum rest-mass density at $t = 0$. The field lines are drawn for $A_\varphi = A_{\varphi,min} + (A_{\varphi,max} - A_{\varphi,min})i/20(i = 1\text{–}19)$, where $A_{\varphi,max}$ and $A_{\varphi,min}$ are the maximum and minimum values of A_φ, respectively, at the given time. The thick solid curves denote the apparent horizon. In the last panel, the field lines are terminated inside the black hole at the excision boundary.

magnetic field near the polar region (see the panels corresponding to time $t = 74.6P_c$ in figure 1).

4.1.2. Resolution study. Four simulations were performed with different resolutions (see figure 2): $N = 250, 300, 400$ and 500. We find that the results converge approximately when $N \gtrsim 400$. On the other hand, results are far from convergent for $N \lesssim 300$. Most importantly, the effect of the MRI is not captured in the two lowest resolution runs, as shown by the behaviour of $|B^x|_{max}$ in figure 2. This is because the wavelength of the fastest growing MRI mode (λ_{max}) is not well resolved for low resolutions. We find that we need a resolution $\Delta/\lambda_{max} \lesssim 0.14$ ($N \gtrsim 400$) in order to resolve the MRI modes. In contrast, the growth
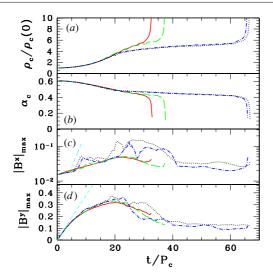
Figure 2. Evolution of the central rest-mass density ρ_c, central lapse α_c, and maximum values of $|B^x|$ and $|B^y|$. $|B^x|_{max}$ and $|B^y|_{max}$ are plotted in units of $\sqrt{\rho_{max}(0)}$. The solid, long-dashed, dot-dash and dotted curves denote the results with $N = 250, 300, 400$ and 500, respectively. The dashed line in (c) represents an approximate slope $\omega = 0.18/P_c$ for the exponential growth rate of the MRI, $\delta B^x \propto e^{\omega t}$. The dashed line in (d) represents the predicted growth of $|B^y|_{max}$ at early times from linear theory.

of B^y by magnetic winding is resolved for all four resolutions. The straight dashed line in figure 2(d) corresponds to the prediction of linear theory for the growth rate due to winding. This slope agrees with the actual growth of $|B^y|_{max}$ in the early (magnetic winding) phase of the simulation, but as back-reaction (magnetic braking) becomes important, the toroidal field begins to saturate. (See [31] for a discussion of the MRI and winding effects in linear theory.)

4.1.3. Evolution with excision. Soon after the formation of the apparent horizon, the simulation becomes inaccurate due to grid stretching and an excision technique is required to follow the subsequent evolution. For details on our excision techniques, see [28–30]. During the excision evolution, we track the irreducible mass of the black hole by computing the area of the apparent horizon $\mathcal{A}_{AH}$ and using $M_{irr} \approx \sqrt{\mathcal{A}_{AH}/16\pi}$. The irreducible mass and the total rest mass outside the apparent horizon are shown in figure 3. The total ADM mass of the final state system, consisting of a BH surrounded by a massive accretion torus, is well defined. In contrast, there is no rigorous definition for the mass of the black hole itself. We obtain a rough estimate following the steps described in [31]. We find that $M_{hole} \sim 0.9M$, where M is the total ADM mass of the system, and $J_{hole}/M_{hole}^2 \sim 0.8$.

The black hole grows at an initially rapid rate following its formation. However, the accretion rate $\dot{M}_0$ gradually decreases and the black hole settles down to a quasi-equilibrium state. By the end of the simulation, $\dot{M}_0$ has decreased to a steady rate of $\approx 0.01 M_0/P_c$, giving an accretion timescale of ~ 10–$20 P_c \approx 5$–10 ms$(M/2.8 M_\odot)$. Also, we find that the specific internal thermal energy in the torus near the surface is substantial because of shock heating. The possibility that this sort of system could give rise to a GRB is discussed in [19].
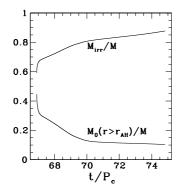
Figure 3. Evolution of the irreducible mass and the total rest-mass outside the apparent horizon. (Here, r_{AH} is the local coordinate radius of the apparent horizon.)
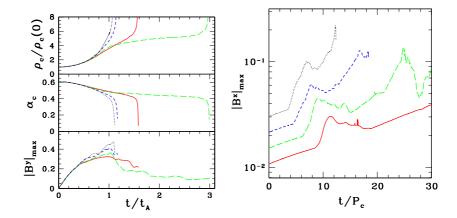

Figure 4. Left: selected parameters plotted against scaled time (t/t_A) for evolutions of star A with four different magnetic field strengths: $C = 1.25 \times 10^{-3}$ (solid lines), $C = 2.5 \times 10^{-3}$ (long-dashed lines), $C = 5.0 \times 10^{-3}$ (short-dashed lines) and $C = 10^{-2}$ (dotted lines). All runs were performed with the same resolution (400^2 zones with outer boundaries at $20M$). When plotted against scaled time, the curves line up at early times ($t \lesssim 0.5t_A = 11P_c$) when the evolution is dominated by magnetic winding. Right: maximum value of $|B^x|$ plotted versus t/P_c for evolutions of star A with four different magnetic field strengths. The line styles are the same as in the left panel. The behaviour of $|B^x|_{max}$ is dominated by the effects of the MRI and thus does not scale with the Alfvén time. The curves corresponding to the two highest values of C (dotted and dashed) terminate at the time when the star collapses

4.2. Star A: comparison of different magnetic field strengths

In order to test the scaling of our results for different values of the initial magnetic field strength, we have examined three other values of C in addition to the value of 2.5×10^{-3} chosen for the results of section 4.1. Namely, we consider $C = \{1.25, 2.5, 5.0, 10\} \times 10^{-3}$, and the results are shown in figure 4. For the portion of the simulations in which magnetic winding dominates, the behaviour is expected to scale with the Alfvén time [22]. In other words, the same profiles should be seen for the same value of t/t_A. From the left panel of figure 4, it is evident that this scaling holds very well for the toroidal field and for the central density and lapse, while $t \lesssim 0.4t_A$. The later evolution is driven mainly by the MRI, which does not scale with the Alfvén time. The scaling also does not hold during the collapse phase,

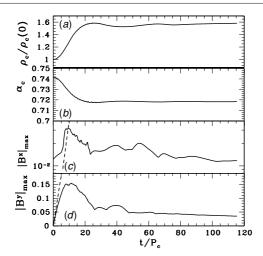**Figure 5.** Evolution of central rest-mass density ρ_c, central lapse α_c, maximum values of $|B^x|$ and $|B^y|$ for star B1. The magnetic fields $|B^x|_{\max}$ and $|B^y|_{\max}$ are plotted in units of $\sqrt{\rho_{\max}(0)}$. Note that the lines become fairly horizontal at late times, indicating that an equilibrium has been reached. The dashed line in (*c*) represents an approximate slope of $\omega = (0.37/P_c)$ for the exponential growth rate of the MRI, $\delta B^x \propto e^{\omega t}$. The dashed line in (*d*) represents the predicted growth of $|B^y|_{\max}$ from linear theory.

when the evolution is no longer quasi-stationary. Though the scaling breaks down at late times in these simulations, the qualitative outcome is the same in all cases. The behaviour of $|B^x|_{\max}$ for these four different values of C is shown in the right panel of figure 4. The sudden sharp rise of $|B^x|_{\max}$ signals the onset of the MRI, and the approximate agreement of the slopes for different values of C indicates that the exponential growth rate of the MRI does not depend on the initial magnetic field strength (as expected from the linear analysis).

4.3. Star B1

Here, we present results for the evolution of star B1 with $C = 2.5 \times 10^{-3}$. This run was performed with resolution 400^2 and outer boundaries located at $4.5R_{\rm eq}$ ($36.4M$). Since this model is not hypermassive, the redistribution of angular momentum through MHD effects will not lead to collapse. However, since this star is ultraspinning and angular momentum is conserved in axisymmetric spacetimes, it cannot relax to a uniform rotation state everywhere unless a significant amount of angular momentum can be dumped into the magnetic field. We find that this model simply seeks out a magnetized equilibrium state which consists of a fairly uniformly rotating core surrounded by a differentially rotating torus.

Figure 5 presents the evolution of some relevant quantities for this case. From the central density and lapse, it is evident that the star has settled into a more compact equilibrium configuration. This is consistent with the expectation that magnetic braking should transfer angular momentum from the core to the outer layers. A brief episode of poloidal magnetic field growth due to the MRI is indicated by the plot of $|B^x|_{\max}$ in figure 5. The instability saturates and quickly dies away, leaving the strength of the poloidal field largely unchanged. Early in the evolution, the maximum value of the toroidal component $|B^y|$ rises due to magnetic winding. This growth saturates at $t \sim 10P_c \sim 0.5t_A$. We note, however, that the toroidal magnetic field is non-zero in the final equilibrium state, though it is no longer growing due to magnetic winding.
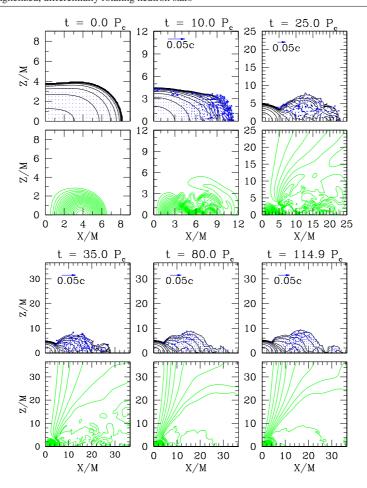
Figure 6. Snapshots of density contours and poloidal magnetic field lines for star B1. The first and third rows show snapshots of the rest-mass density contours and velocity vectors on the meridional plane. The second and fourth rows show the field lines (lines of constant A_φ) for the poloidal magnetic field at the same times as the first and third rows. The density contours are drawn for $\rho_0/\rho_{\max}(0) = 10^{-0.36i-0.09}(i = 0\text{--}10)$. The field lines are drawn for $A_\varphi = A_{\varphi,\min} + (A_{\varphi,\max} - A_{\varphi,\min})i/20(i = 1\text{--}19)$, where $A_{\varphi,\max}$ and $A_{\varphi,\min}$ are the maximum and minimum values of A_φ respectively at the given time. Note that the field lines and the density contours show little change for $t \gtrsim 35 P_c$, indicating that the star has settled down to an equilibrium state.

Snapshots of the evolution in the x–z plane are shown in figure 6. The density contours for times $t = 0$ through $25.0 P_c$ show that angular momentum redistribution leads to the formation of a more compact star surrounded by a torus. At $t = 10 P_c$, the distortions of the magnetic field lines due to the MRI are clearly visible. As the disc expands, magnetic field lines attached to this low density material open outward, eventually leading to the field structure seen in the last three times shown in figure 6, for which some field lines are still confined inside the star while others have become somewhat collimated along the z-axis. For $t \gtrsim 35 P_c$, the density contours and poloidal magnetic field lines change very little, indicating that the system has reached an equilibrium state which is quite different from the initial state. We note that a significant toroidal field persists at late times when the system has essentially settled down to a final state. In addition, the final configuration also has significant differential rotation, especially in the
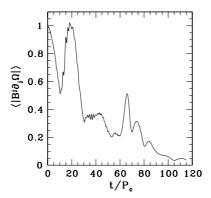
Figure 7. Evolution of $\langle |B^j \partial_j \Omega| \rangle$ (normalized to unity at $t = 0$). Note that this quantity drops toward zero at late time, indicating that the star is driven to a differentially rotating equilibrium state in which Ω is constant along the magnetic field lines.
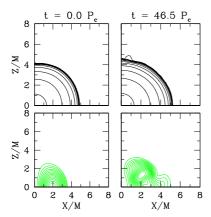

Figure 8. Snapshots of the rest-mass density contours and poloidal magnetic field lines for star B2 at times $t = 0$ and $t = 46.5 P_c$. The first row shows snapshots of the rest-mass density contours on the meridional plane. The second row shows the corresponding field lines for the poloidal magnetic field at the same times. The density contours are drawn for $\rho_0/\rho_{max}(0) = 10^{-0.36i-0.09} (i = 0–10)$, where $\rho_{max}(0)$ is the maximum rest-mass density at $t = 0$. The field lines are drawn for $A_\varphi = A_{\varphi,min} + (A_{\varphi,max} - A_{\varphi,min})i/15 (i = 1–14)$, where $A_{\varphi,max}$ and $A_{\varphi,min}$ are the maximum and minimum values of A_φ, respectively, at the given time. The meridional components of the velocity (which are zero initially) at $t = 46.5 P_c$ are very small and so are not shown here.

outer layers. However, this differential rotation no longer winds up the magnetic field lines (i.e., the toroidal field strength does not grow). This is because the rotation profile has adjusted so that Ω is approximately constant along magnetic field lines. This is demonstrated in figure 7, which shows that the density-weighted average of the quantity $B^j \partial_j \Omega$ approaches zero at late times. Since the rotation profile is adapted to the magnetic field structure, a stationary final state is reached which allows differential rotation and a non-zero toroidal field.

4.4. Star B2

Both stars B1 and B2 are non-hypermassive. However, star B1 is ultraspinning, whereas B2 is normal. We evolve B2 with a seed magnetic field strength $C = 2.5 \times 10^{-3}$. Our simulation shows that this star evolves to a uniformly rotating configuration with little structural change.

Figure 8 shows the density contours and poloidal magnetic field at the initial time ($t = 0$) and at $t = 46.5P_c \approx 5.8t_A$. We see that the density profile of the star does not change appreciably. This is not surprising since the main effect of the MHD processes is to redistribute the angular momentum inside the star. However, the rotational kinetic energy of star B2 is not very large (the initial $T/|W| = 0.040$). Hence, the change of the centrifugal force inside the star as a result of angular momentum transport does not disturb the initial equilibrium significantly, unlike the cases of stars A and B1.

5. Discussion and conclusions

We have discussed in detail the evolution of magnetized HMNSs as first reported in [18, 19]. In addition, we have performed simulations of two differentially rotating, but non-hypermassive, neutron star models with the same initial magnetic field geometry. These simulations have revealed a rich variety of behaviour with possible implications for astrophysically interesting systems such as binary neutron star remnants, nascent neutron stars and GRBs, where magnetic fields and strong gravity both play important roles.

The hypermassive model considered here, star A, collapses to a BH due to the influence of the initial seed magnetic field. The early phase of evolution is dominated by magnetic winding, which proceeds until the back-reaction on the fluid becomes strong enough that the growth of the toroidal field ceases. This happens after roughly one Alfvén time. After several rotation periods, we also see the effects of the MRI, which leads to turbulence. Eventually, the inner core of star A becomes unstable and collapses to a BH. Surrounding the BH, a significant amount of material remains in a magnetized torus which has been heated considerably by shocks resulting from the turbulent motions of the fluid. This final state consisting of a BH surrounded by a massive, hot accretion disc may be capable of producing highly relativistic outflows and a fireball (either through $\nu - \bar{\nu}$ annihilation or MHD processes) and is hence a promising candidate for the central engine of short-hard GRBs. This model predicts that such GRBs should accompany a burst of gravitational radiation and neutrino emission from the HMNS delayed collapse.

The behaviour of the non-hypermassive, ultraspinning star B1 under the influence of a seed magnetic field is quite different. Magnetic braking and the MRI operate in this model as well, leading to a mild contraction of the inner core and the expansion of the outer layers into a high angular momentum torus-like structure. The final state consists of a fairly uniformly rotating core surrounded by a differentially rotating torus. The remaining differential rotation does not shear the magnetic field lines, so that the toroidal field settles down. On the other hand, the normal star B2 simply evolves to a uniformly rotating configuration.

Two issues in particular warrant further study. The first is the scaling behaviour of our solutions. We begin our simulations with a seed magnetic field which, though far too weak to be dynamically important, may be significantly larger than magnetic fields present in HMNSs formed through stellar collapse or a binary neutron star merger. We have demonstrated that, by varying the strength of the initial magnetic field through a factor of ~ 3 (see figure 4), our evolution obeys the expected scaling during the magnetic winding phase, and the qualitative outcome of the simulations remains the same. However, since the MRI grows on a timescale $\sim$few $\times P_c$ regardless of the initial magnetic field strength, it is possible that, for very weak initial fields, the effects of the MRI could dominate the evolution long before the effects of magnetic braking become important. In this case, the scaling of our numerical results with the Alfvén time (relevant for magnetic winding) may break down.

Another concern is the effect on our evolutions of relaxing the axisymmetry assumption. Rapidly and differentially rotating neutron stars may be subject to bar and/or one-armed

spiral mode instabilities which could affect the dynamics (though star A was shown in [7, 25] to be stable against such instabilities, at least on dynamical timescales). Additionally, the development of the MRI in 2D differs from the 3D case [32]. Turbulence arises and persists more readily in 3D due to the lack of symmetry [33, 34]. However, McKinney and Gammie [35] have performed axisymmetric simulations of magnetized tori accreting onto Kerr BHs and have found good quantitative agreement with the 3D results of De Villiers and Hawley [36] on the global features of the evolution. Though simulations in full 3D will eventually be necessary to capture the full behaviour of magnetized HMNSs, the 2D results presented here likely provide (at least) a good qualitative picture.

Acknowledgments

References

[1] Zwerger T and Müller E 1997 *Astron. Astrophys.* **320** 209
[2] Rampp M, Müller E and Ruffert M 1998 *Astron. Astrophys.* **332** 969
    Dimmelmeier H, Font J A and Müller E 2002 *Astron. Astrophys.* **388** 917
    Dimmelmeier H, Font J A and Müller E 2002 *Astron. Astrophys.* **393** 523
    Shibata M and Sekiguchi Y 2004 *Phys. Rev.* D **69** 084024
    Ott C D, Burrows A, Livne E and Walder R 2004 *Astrophys. J.* **600** 834
[3] Liu Y T and Lindblom L 2001 *Mon. Not. R. Astron. Soc.* **324** 1063
    Liu Y T 2002 *Phys. Rev.* D **65** 124003
[4] Rasio F A and Shapiro S L 1994 *Astrophys. J.* **432** 242
    Rasio F A and Shapiro S L 1999 *Class. Quantum Grav.* **16** R1
[5] Shibata M and Uryū K 2000 *Phys. Rev.* D **61** 064001
[6] Faber J A and Rasio F A 2000 *Phys. Rev.* D **62** 064012
[7] Baumgarte T W, Shapiro S L and Shibata M 2000 *Astrophys. J. Lett.* **528** L29
[8] Morrison I A, Baumgarte T W, Shapiro S L and Pandharipande V R 2004 *Astrophys. J.* **610** 941
[9] Shibata M, Taniguchi K and Uryū K 2003 *Phys. Rev.* D **68** 084020
[10] Shibata M, Taniguchi K and Uryū K 2005 *Phys. Rev.* D **71** 084021
[11] Shibata M and Taniguchi K 2006 *Phys. Rev.* D **73** 064027
[12] Zhang B and Mészáros P 2004 *Int. J. Mod. Phys.* A **19** 2385
    Piran T 2005 *Rev. Mod. Phys.* **76** 1143
[13] Narayan R, Paczyński B and Piran T 1992 *Astrophys. J. Lett.* **395** L83
    Ruffert M and Janka H-T 1999 *Astron. Astrophys.* **344** 573
[14] Duez M D, Liu Y T, Shapiro S L and Stephens B C 2005 *Phys. Rev.* D **72** 024028
[15] Shibata M and Sekiguchi Y-I 2005 *Phys. Rev.* D **72** 044014
[16] Antón L, Zanotti O, Miralles J A, Martí J M, Ibáñez J M, Font J A and Pons J A 2006 *Astrophys. J.* **637** 296
[17] Anderson M, Hirschmann E W, Liebling S L and Neilsen D 2006 *Class. Quantum Grav.* **23** 6503
    Neilsen D, Hirschmann E W and Millward R S 2006 *Class. Quantum Grav.* **23** S505
[18] Duez M D, Liu Y T, Shapiro S L, Shibata M and Stephens B C 2006 *Phys. Rev. Lett.* **96** 031101 (*Preprint* astro-ph/0510653)
[19] Shibata M, Duez M D, Liu Y T, Shapiro S L and Stephens B C 2006 *Phys. Rev. Lett.* **96** 031102 (*Preprint* astro-ph/0511142)
[20] Velikhov V P 1959 *Sov. Phys.—JETP* **36** 995
    Chandrasekhar S 1960 *Proc. Natl Acad. Sci. USA* **46** 253

[21] Balbus S A and Hawley J F 1998 *Rev. Mod. Phys.* **70** 1
[22] Shapiro S L 2000 *Astrophys. J.* **544** 397
      Cook J N, Shapiro S L and Stephens B C 2003 *Astrophys. J.* **599** 1272
      Liu Y T and Shapiro S L 2004 *Phys. Rev.* D **69** 104030
[23] Cook G C, Shapiro S L and Teukolsky S A 1994 *Astrophys. J.* **422** 227
[24] Shibata M, Baumgarte T W and Shapiro S L 2000 *Astrophys. J.* **542** 453
[25] Duez M D, Liu Y T, Shapiro S L and Stephens B C 2004 *Phys. Rev.* D **69** 104030
[26] Alcubierre M, Brandt S, Brügmann B, Holz D, Seidel E, Takahashi R and Thornburg J 2001 *Int. J. Mod. Phys.*
      D **10** 273
[27] Shibata M and Nakamura T 1995 *Phys. Rev.* D **52** 5428
      Baumgarte T W and Shapiro S L 1999 *Phys. Rev.* D **59** 024007
[28] Alcubierre M and Brügmann B 2001 *Phys. Rev.* D **63** 104006
[29] Duez M D, Shapiro S L and Yo H-J 2004 *Phys. Rev.* D **69** 104016
[30] Yo H-J, Baumgarte T W and Shapiro S L 2002 *Phys. Rev.* D **66** 084026
[31] Duez M D, Liu Y T, Shapiro S L, Shibata M and Stephens B C 2006 *Phys. Rev.* D **73** 104015
[32] Hawley J F, Gammie C F and Balbus S A 1995 *Astrophys. J.* **440** 742
      Hawley J F 2000 *Astrophys. J.* **528** 462
[33] Moffatt H K 1978 *Magnetic Field Generation in Electrically Conducting Fluids* (Cambridge: Cambridge
      University Press)
[34] Hawley J F and Balbus S A 1992 *Astrophys. J.* **400** 595
[35] McKinney J C and Gammie C F 2004 *Astrophys. J.* **611** 977
[36] Villiers J-P De, Hawley J F, Krolik J H and Hirose S 2005 *Astrophys. J.* **620** 878